Springer

Acta Mechanica Sinica

CrossMark click for updates

• RESEARCH PAPER •

Acta Mech. Sin., Vol. 39, 423179 (2023)
https://doi.org/10.1007/s10409-023-23179-x

3D computational grains with embedded fibers for the direct micromechanical modeling of fiber composites

Yezeng Huang[1,2], Junbo Wang[2,3*], Mingjing Li[1,2], Guannan Wang[4], Leiting Dong[1,2*], and Satya N. Atluri[5]

[1] *Tianmushan Laboratory, Hangzhou 310023, China;*
[2] *School of Aeronautic Science and Engineering, Beihang University, Beijing 100191, China;*
[3] *Shenyang Aircraft Design Institute Yangzhou Collaborative Innovation Institute Co., Ltd., Yangzhou 225000, China;*
[4] *Department of Civil Engineering, Zhejiang University, Hangzhou 310058, China;*
[5] *Department of Mechanical Engineering, Texas Tech University, Lubbock 79409, USA*

Received May 18, 2023; accepted May 24, 2023; published online August 25, 2023

For the integrated design of composite material and structures, it is essential to have an effective micromechanical numerical tool to link macroscopic material properties to microstructural configurations. In this paper, 3D computational grains (CGs) with embedded fibers are proposed for the first time, for the direct micromechanical modeling of fiber composites. The microstructure of a unidirectional lamina with random fibers can be assembled by many CGs, and the stiffness matrix of each CG with an embedded fiber can be directly computed by combining two new algorithms. On one hand, a new kind of Trefftz trial displacement field based on scaled cylindrical harmonics is independently assumed, in addition to inter-elemental displacement interpolations with surface nodal degrees of freedom (DoFs). On the other hand, a new kind of multi-field boundary variational principle is proposed to relate independently assumed Trefftz fields to nodal DoFs and to derive the stiffness matrix. Numerical examples demonstrate that without the traditional fine meshing, accurate distribution of micro-stresses in a representative volume element (RVE) with thousands of fibers can be directly computed, and the equivalent orthotropic properties of fiber composites can be predicted. This is also the first time that a three-dimensional finite element with an embedded fiber is developed.

Computational grains, Fiber composite, Multi-field variational principle, Cylindrical harmonics, Micromechanics

Citation: Y. Huang, J. Wang, M. Li, G. Wang, L. Dong, and S. N. Atluri, 3D computational grains with embedded fibers for the direct micromechanical modeling of fiber composites, Acta Mech. Sin. 39, 423179 (2023), https://doi.org/10.1007/s10409-023-23179-x

1. Introduction

During the past decades, fiber composites have been widely used in lightweight structures in mechanical, automotive, and aerospace engineering, due to their excellent mechanical properties (e.g., specific stiffness and specific strength) and the strong designability [1-3]. The weight-reduction potential of fiber composite structures can be better realized by the integrated structure-material design and optimization [4]. In order to achieve this goal, it is necessary to have an accurate and efficient tool to model the micromechanical behavior and to predict the equivalent properties of fiber composites based on their microstructures.

Several analytical methods have been proposed for predicting the equivalent properties of fiber composites. To name a few, Hill [5] and Hashin [6] derived the upper and lower bounds of the five independent effective elastic moduli of fiber composites; Hill [7] derived the expressions of the overall moduli of fiber composites by the self-consistent model; Benveniste et al. [8] proposed a micromechanical model for predicting the micro stress fields and the effective properties of fiber composites, based on the "average stress in the matrix" concept of Mori and Tanaka

*Corresponding authors. E-mail addresses: junbowang@outlook.com (Junbo Wang); ltdong@buaa.edu.cn (Leiting Dong)
Executive Editor: Xiaoding Wei

[9] and the equivalent inclusion idea of Eshelby [10]. Such analytical methods have advantages thanks to their explicit or semi-expressions of the effective properties, while their accuracies are not generally guaranteed. For example, the moduli may be under-estimated for composites with high volume fractions of fibers [11].

Numerical micromechanical methods have higher accuracy and better generality as compared to analytical methods. With a representative volume element (RVE), microscopic stresses and overall material properties can be computed by the finite element method (FEM) [12-16]. FEM is also employed in multi-scale analysis frameworks to model the responses of composite structures (e.g., elastic deformation [17], buckling [18], and damage [19-21]), coupling the micro-, meso- and macro-scale FEM models. However, in order to capture the fields around the interface of the fiber and the matrix accurately, very fine FEM-discretization is needed, which necessitates considerable human-labors and leads to high computational costs [22]. Such burden of meshing and computation will become highly serious, when modeling a 3D RVE with a large number of fibers [23,24].

To overcome such problems, Voronoi cell finite element method (VCFEM) [25,26] has been proposed. VCFEMs are based on the hybrid stress framework of Pian [27], with independently assumed stress fields in each element. With such an approach, a 2D RVE can be discretized into multi-sided Voronoi cells, each of which contains one inclusion, thus reducing the laborious FEM meshing process [28]. VCFEMs are also extended to 3D versions with embedded inclusions, to model particulate-reinforced composites [29]. However, for fiber composites, only two-dimensional VCFEMs are developed to simulate the transverse mechanical behavior [30,31], and no 3D VCFEMs with embedded fibers have been reported heretofore.

Another numerical method, named computational grains (CGs), has been developed by Dong and Atluri for the 3D modeling of the micromechanical behaviors of particulate composites [32,33], nanocomposites [34], three-phase materials [35], piezoelectric materials [36], and viscoelastic behavior of composites [37]. In such a framework, independently assumed Trefftz trial displacement fields for various physical problems are derived to satisfy the governing equations a-priori, so that the stress distribution can be predicted more accurately. Moreover, only boundary integrals are needed to compute the stiffness matrix of each CG, which significantly reduces the computational cost. Based on extensive numerical experiments of various physical responses for various materials, CGs exhibit the high computational efficiency and accuracy for the predictions of not only homogenized moduli but also localized stress concentrations even for RVEs with a large number of randomly-distributed inclusions.

However, no previous studies have been reported before for developing FEMs with embedded fibers, which can be quite useful for the micromechanical modeling of fiber composites, based on the experiences to our previous works. For this reason, in this study, 3D CGs with embedded fibers are developed for the first time, and verified by a large number of numerical examples.

In order to extend CGs with embedded particles to ones with embedded fibers, two problems need to be solved. Firstly, when the Trefftz trial displacement fields in the matrix and in each fiber are assumed in terms of Papkovich-Neuber (P-N) solutions, the spherical harmonics or ellipsoidal harmonics used for particulate composites are not suitable anymore. Instead, cylindrical harmonics are employed herein as the P-N potentials for fiber composites. It should be noticed that the cylindrical harmonics contain severely ill-conditioned terms, such as Bessel functions, power functions, and hyperbolic functions. In this study, a new scheme of scaling the cylindrical harmonics is also proposed which can effectively avoid the ill-conditioning problems.

On the other hand, the compatibility condition between the independent assumed fields in the CGs of fiber composites is not the same as that in particulate composites. In particulate composites, the inclusions are completely wrapped in the matrix, thus at the matrix/inclusion interfaces, only the displacement continuity and the traction reciprocity conditions need to be considered. However, in fiber composites, the upper and lower surfaces of the embedded fibers are not covered by the matrix. Thus, on the upper and lower surfaces, in addition to the inter-CG displacement continuity and the traction reciprocity conditions, the prescribed displacement/traction boundary conditions should also be satisfied. Therefore, for CGs with embedded fibers, a new multi-field boundary variational principle has been developed in this paper, the stationarity of which leads to the revised interface/boundary conditions, to derive the stiffness matrix of each CG with an embedded fiber.

Verified by several typical numerical examples, the proposed CGs have been proved to be an efficient and accurate numerical method for predicting the equivalent material properties and the stress fields of fiber composites. Moreover, the computational efficiency of the proposed CGs is further enhanced by using parallel computation techniques, by which a RVE with thousands of fibers can be solved within hours on a regular desktop PC. In the future, in a multi-scale analysis framework, the CGs in the micro-scale can be coupled with FEMs at the laminate and structural scale, for the integrated modeling and design of composite material and structures. This will be demonstrated in our future studies.

The rest of this paper is organized as follows: Sect. 2 introduces the governing equations for both the fibers and

the matrix in the CGs of fiber composites. In Sect. 3, Trefftz trial displacement fields with scaled cylindrical harmonics as P-N potentials are derived. Section 4 introduces the new multi-field boundary variational principle developed in this work and the element stiffness matrices derived accordingly. In Sect. 5, the accuracy and efficiency of the proposed CGs are discussed with comparisons with exact solutions and experimental results. The efficiency of CGs with simple parallelization is also discussed. In Sect. 6, this study is completed with some conclusion remarks.

2. Governing equations for the matrix and the fiber of a CG

For a RVE containing a large number of fibers, as shown in Fig. 1(a), it can be discretized into CGs by Voronoi diagram, and each of the CGs contains a fiber in its domain, as shown in Fig. 1(b).

As shown in Fig. 1(c), an arbitrary CG Ω^e with its outer boundary $\partial\Omega^e$ is considered. The outer boundary of the CG can be further classified as S_u^e, S_t^e, ρ^e, which represent the displacement-prescribed boundary, the traction-prescribed boundary, and the inter-CG boundary, respectively. Ω_f^e and Ω_m^e denote the domains of the fiber and the matrix, and $\partial\Omega_f^e$, $\partial\Omega_m^e$ denote the boundaries of Ω_f^e and Ω_m^e, respectively. Γ^e is the fiber/matrix interface. Thus, we have the following relationship: $\Omega_f^e \cup \Omega_m^e = \Omega^e$, and $\partial\Omega_f^e \cap \partial\Omega_m^e = \Gamma^e$.

A linear elastic CG is considered in the Cartesian coordinates. σ_{ij}, ε_{ij}, u_i denote the components of the stress tensor, strain tensor, and displacement vector, respectively. $\overline{f}_i$, $\overline{u}_i$, $\overline{t}_i$ are the components of the body force, boundary displacement, and boundary traction vector. C_{ijkl}, S_{ijkl} denote the components of the stiffness tensor and the flexibility tensor respectively. The equilibrium equations, constitutive equations, strain-displacement relationship, as well as boundary conditions, can be expressed as

$$\sigma_{ij,j}^k + \overline{f}_i^k = 0, \tag{1}$$

$$\sigma_{ij}^k = C_{ijkl}^k \varepsilon_{kl}^k \Leftrightarrow \varepsilon_{ij}^k = S_{ijkl}^k \sigma_{kl}^k, \tag{2}$$

$$\varepsilon_{ij}^k = \frac{1}{2}\left(u_{i,j}^k + u_{j,i}^k\right) \equiv u_{(i,j)}^k, \tag{3}$$

$$u_i^k = \overline{u}_i \text{ at } S_u, \tag{4}$$

$$n_j \sigma_{ij}^k = \overline{t}_i \text{ at } S_t, \tag{5}$$

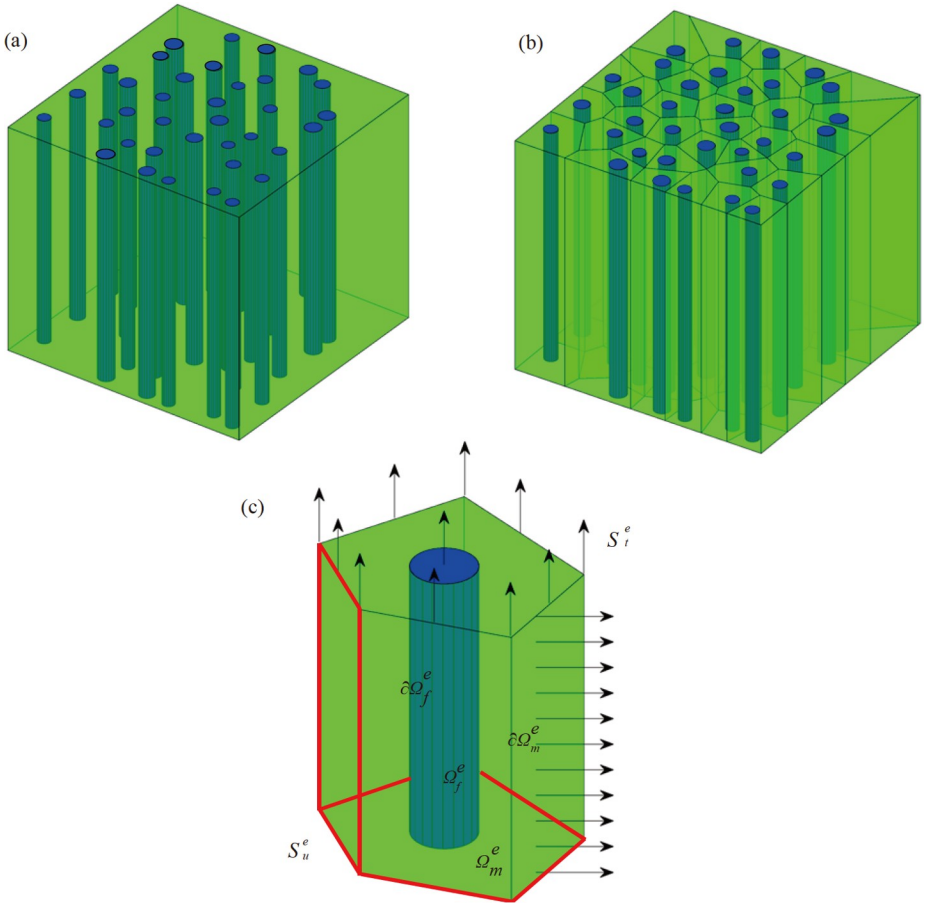

Figure 1 Illustrations of (a) a RVE with many fibers; (b) the RVE discretized into CGs; (c) an arbitrary CG containing a fiber.

where the superscript $k = m, f$ denotes the domain of the matrix and the fiber respectively, and $()_{,i}$ denotes the differentiation with respect to x_i.

For 3D isotropic materials in which body force is negligible, equilibrium equations (Eq. (1)) can be re-expressed as the Navier's equation, by combining constitutive equations (Eq. (2)) and geometric equations (Eq. (3)):

$$(\lambda^k+\mu^k)u^k_{j,ji}+\mu^k\Delta u_i^k=0, \tag{6}$$

where $\lambda^k=\dfrac{E^k\nu^k}{(1+\nu^k)(1-2\nu^k)}$, $\mu^k=G^k=\dfrac{E^k}{2(1+\nu^k)}$ denote the Lame constants for the matrix/fiber in the CG.

It should also be noted that the displacement continuity and traction reciprocity need to be implemented at Γ^e and ρ^e in each CG:

$$u_i^m=u_i^f \text{ at } \Gamma^e, \tag{7}$$

$$n_j\sigma_{ij}^m+n_j\sigma_{ij}^f=0 \text{ at } \Gamma^e, \tag{8}$$

$$\left(u_i^m\right)^+=\left(u_i^m\right)^- \text{ at } \rho^e, \tag{9}$$

$$\left(n_j\sigma_{ij}^m\right)^++\left(n_j\sigma_{ij}^m\right)^-=0 \text{ at } \rho^e, \tag{10}$$

where n_j is the unit outer normal vector of the surface.

3. Trefftz trial displacement fields within CGs

3.1 Papkovich-Neuber solutions

To satisfy the Navier's equation shown in Eq. (6), the trial displacement fields in each CG can be assumed in the form of PN solutions [38]:

$$\mathbf{u}=[4(1-\nu)\mathbf{B}-\nabla(\mathbf{R}\cdot\mathbf{B}+\mathbf{B}_0)]/(2G), \tag{11}$$

where $\mathbf{R}=x_i\mathbf{e}_i$ denotes the position vector, and $\mathbf{B}$, $\mathbf{B}_0$ are harmonic vectors and scalars, which are also named as PN potentials, whose Laplace operator vanishes.

It has been proven by M. G. Slobodyansky that for a simply-connected domain:

$$\mathbf{u}=[4(1-\nu)\mathbf{B}+\mathbf{R}\cdot\nabla\mathbf{B}-\mathbf{R}\nabla\cdot\mathbf{B}]/(2G) \tag{12}$$

is a complete trial displacement field for any ν, without the use of harmonic scalars.

Besides, it is also proven that

$$\mathbf{u}=[4(1-\nu)\mathbf{B}-\nabla\mathbf{R}\cdot\mathbf{B}]/(2G) \tag{13}$$

is complete for the external region to a closed surface for any ν, and for the simply-connected domain when $\nu\neq0.25$. Readers can refer to Ref. [38] for the detailed explanation of the completeness of the P-N solutions.

The harmonic vector $\mathbf{B}$ needs to be further represented using cylindrical harmonics for the convenience of further calculations, which will be introduced in the next subsection.

3.2 Cylindrical harmonics as Papkovich-Neuber potentials

As shown in Fig. 2, consider a position vector in Cartesian coordinate $[x_1,x_2,x_3]$ and the corresponding cylindrical coordinate $[q^1,q^2,q^3]=[r,\theta,z]$, and they have the relationship as

$$x_1=r\cos\theta,\ x_2=r\sin\theta,\ x_3=z. \tag{14}$$

The base vectors $\mathbf{e}_1=\mathbf{e}_r$, $\mathbf{e}_2=\mathbf{e}_\theta$, $\mathbf{e}_3=\mathbf{e}_z$ are in the directions of the radius of circles, the tangents to circles and z axis, respectively. $\mathbf{R}=x_i\mathbf{e}_i$ denotes the position vector. Now we have

$$\begin{aligned}&\frac{\partial x_1}{\partial r}=\cos\theta,\ \frac{\partial x_1}{\partial\theta}=-r\sin\theta,\ \frac{\partial x_1}{\partial z}=0,\\&\frac{\partial x_2}{\partial r}=\sin\theta,\ \frac{\partial x_2}{\partial\theta}=r\cos\theta,\ \frac{\partial x_2}{\partial z}=0,\\&\frac{\partial x_3}{\partial r}=0,\ \frac{\partial x_3}{\partial\theta}=0,\ \frac{\partial x_3}{\partial z}=1,\end{aligned} \tag{15}$$

and

$$\begin{aligned}&\frac{\partial q^s}{\partial x_k}=\frac{1}{H_s^2}\frac{\partial x_k}{\partial q^s},\\&\frac{\partial\mathbf{R}}{\partial q^s}\cdot\frac{\partial\mathbf{R}}{\partial q^t}=\delta_{st}H_sH_t,\end{aligned} \tag{16}$$

where $H_1=H_r=1$, $H_2=H_\theta=r$, $H_3=H_z=1$. These parameters are called Lame's coefficients. The orthonormal base vectors of the cylindrical coordinates can be defined as

$$\mathbf{a}_s=\frac{1}{H_s}\frac{\partial\mathbf{R}}{\partial q^s}, \tag{17}$$

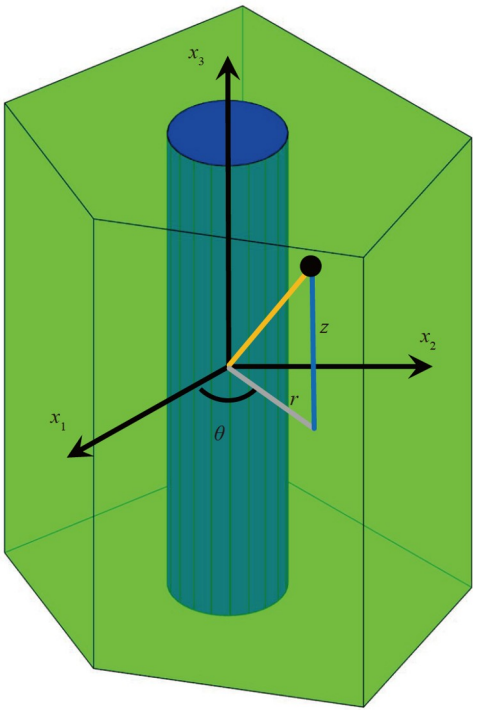

Figure 2 Schematic diagram of cylindrical coordinates.

we have

$$\begin{aligned}&\frac{\partial \mathbf{a}_r}{\partial r}=0,\ \frac{\partial \mathbf{a}_r}{\partial \theta}=\mathbf{a}_\theta,\ \frac{\partial \mathbf{a}_r}{\partial z}=0,\\&\frac{\partial \mathbf{a}_\theta}{\partial r}=0,\ \frac{\partial \mathbf{a}_\theta}{\partial \theta}=-\mathbf{a}_r,\ \frac{\partial \mathbf{a}_\theta}{\partial z}=0,\\&\frac{\partial \mathbf{a}_z}{\partial r}=0,\ \frac{\partial \mathbf{a}_z}{\partial \theta}=0,\ \frac{\partial \mathbf{a}_z}{\partial z}=0.\end{aligned}\tag{18}$$

The Laplace operator of a scalar ψ in cylindrical coordinate can be obtained as

$$\begin{aligned}\nabla^2\psi=\nabla\cdot\nabla\psi&=\frac{1}{H_s}\mathbf{a}_s\frac{\partial}{\partial q^s}\cdot\frac{1}{H_t}\mathbf{a}_t\frac{\partial\psi}{\partial q^t}\\&=\frac{1}{r}\frac{\partial}{\partial r}\left(r\frac{\partial\psi}{\partial r}\right)+\frac{1}{r^2}\frac{\partial^2\psi}{\partial\theta^2}+\frac{\partial^2\psi}{\partial z^2}=0.\end{aligned}\tag{19}$$

The above Laplace equation can be simplified with the use of the separation of variables, by assuming $\psi(r,\theta,z)=f(r)g(\theta)h(z)$ with λ and κ as separating constants, the details of which can be found in Appendix. The following three equations should be satisfied:

$$\frac{\partial^2 h(z)}{\partial z^2}+\lambda h(z)=0,\tag{20}$$

$$\frac{\partial^2 g(\theta)}{\partial\theta^2}+\kappa g(\theta)=0,\tag{21}$$

$$\frac{\partial^2 f(r)}{\partial r^2}+\frac{1}{r}\frac{\partial f(r)}{\partial r}+\left(-\lambda-\frac{\kappa}{r^2}\right)f(r)=0.\tag{22}$$

Equations (20)-(22) can be solved separately depending on the values of λ and κ. By letting $\lambda=\pm m^2$ and $\kappa=\pm n^2$, where m and n are positive integers, the general solutions of the Laplace equation can be divided into the non-singular form $\psi_{\text{in}}(r,\theta,z)$ and singular form $\psi_{\text{ex}}(r,\theta,z)$ for the programming of CGs.

The non-singular solution of a cylinder is shown as

$$\begin{aligned}\psi_{\text{in}}(r,\theta,z)=&a_{01}+a_{02}z+\sum_{m=1}^{\infty}\left\{e_{1m}r^m\cos(m\theta)+e_{2m}r^m\sin(m\theta)+e_{3m}zr^m\cos(m\theta)+e_{4m}zr^m\sin(m\theta)\right\}\\&+\sum_{n=1}^{\infty}\left\{c_{1n}\cosh(nz)J_0(nr)+c_{2n}\sinh(nz)J_0(nr)+c_{3n}\cos(nz)I_0(nr)+c_{4n}\sin(nz)I_0(nr)\right\}\\&+\sum_{n=1}^{\infty}\sum_{m=1}^{\infty}\left\{d_{1mn}\cos(m\theta)\cosh(nz)J_m(nr)+d_{2mn}\sin(m\theta)\cosh(nz)J_m(nr)+d_{3mn}\cos(m\theta)\sinh(nz)J_m(nr)\right.\\&+d_{4mn}\sin(m\theta)\sinh(nz)J_m(nr)+d_{5mn}\cos(m\theta)\cos(nz)I_m(nr)+d_{6mn}\sin(m\theta)\cos(nz)I_m(nr)\\&\left.+d_{7mn}\cos(m\theta)\sin(nz)I_m(nr)+d_{8mn}\sin(m\theta)\sin(nz)I_m(nr)\right\},\end{aligned}\tag{23}$$

where J_m and I_m are the mth order Bessel function of the first kind and the modified Bessel function of the first kind, respectively.

And the singular solution is written as

$$\begin{aligned}\psi_{\text{ex}}(r,\theta,z)=&a_{03}\ln r+a_{04}z\ln r+\sum_{m=1}^{\infty}\left\{e_{5m}r^{-m}\cos(m\theta)+e_{6m}r^{-m}\sin(m\theta)+e_{7m}zr^{-m}\cos(m\theta)+e_{8m}zr^{-m}\sin(m\theta)\right\}\\&+\sum_{n=1}^{\infty}\left\{c_{5n}\cosh(nz)Y_0(nr)+c_{6n}\sinh(nz)Y_0(nr)+c_{7n}\cos(nz)K_0(nr)+c_{8n}\sin(nz)K_0(nr)\right\}\\&+\sum_{n=1}^{\infty}\sum_{m=1}^{\infty}\left\{d_{9mn}\cos(m\theta)\cosh(nz)Y_m(nr)+d_{10mn}\sin(m\theta)\cosh(nz)Y_m(nr)\right.\\&+d_{11mn}\cos(m\theta)\sinh(nz)Y_m(nr)+d_{12mn}\sin(m\theta)\sinh(nz)Y_m(nr)\\&+d_{13mn}\cos(m\theta)\cos(nz)K_m(nr)+d_{14mn}\sin(m\theta)\cos(nz)K_m(nr)\\&\left.+d_{15mn}\cos(m\theta)\sin(nz)K_m(nr)+d_{16mn}\sin(m\theta)\sin(nz)K_m(nr)\right\},\end{aligned}\tag{24}$$

where Y_m and K_m are the mth order Bessel function of the second kind and the modified Bessel function of the second kind, respectively. The Bessel functions are shown in Fig. 3.

3.3 Scaling cylindrical harmonics to avoid Ill-conditioning

Several terms in the cylindrical harmonics in Eqs. (23) and (24), such as r^m, r^{-m}, $\sinh(nz)$, $\cosh(nz)$, $I_m(nr)$, $K_m(nr)$, will cause the ill-conditioning of the resulting system of equations. In order to avoid solving ill-conditioned equations, three characteristic lengths $r_{\max}$, $r_{\min}$, and z_0 are introduced. With a local cylindrical coordinate system with its origin located at the mid-height on the axis of the cylindrical fiber, $r_{\max}$ and $r_{\min}$ denote the maximum and minimum values of the cylindrical coordinate r, and z_0 is half of the height of the fiber embedded in the CG, as shown in Fig. 4.

Thus, in the case of the scaled cylindrical harmonics $\frac{z}{z_0}$, $\left(\frac{r}{r_{\max}}\right)^m$, $\left(\frac{r}{r_{\min}}\right)^{-m}$, $\frac{\sinh(nz)}{\sinh(nz_0)}$, $\frac{\cosh(nz)}{\cosh(nz_0)}$, $\frac{I_m(nr)}{I_m(nr_{\max})}$, and

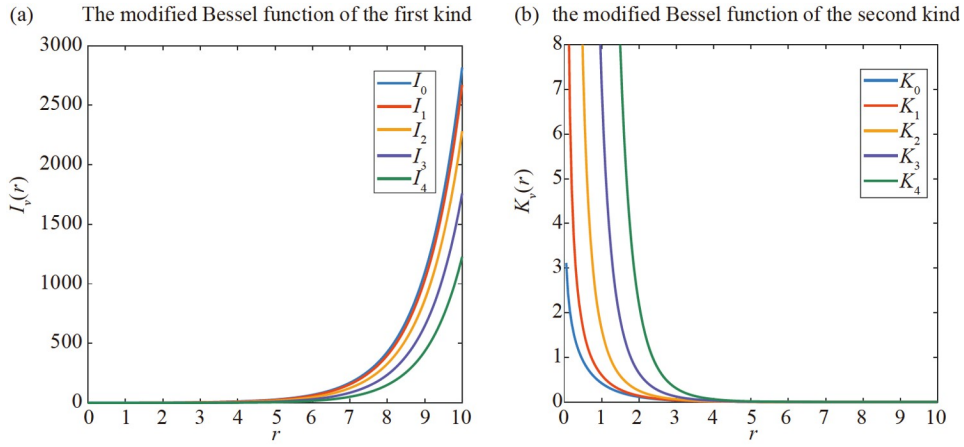

Figure 3 Schematic diagrams of (a) the modified Bessel function of the first kind, (b) the modified Bessel function of the second kind.

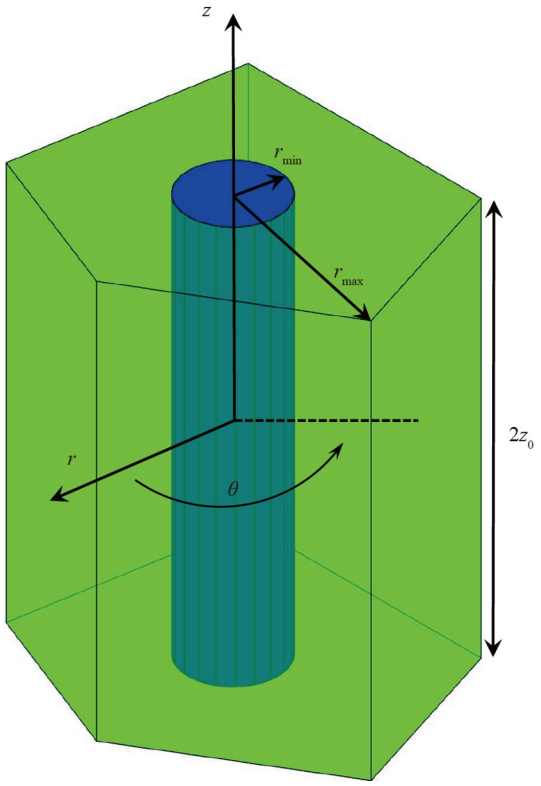

Figure 4 Schematic diagram of the characteristic lengths in a CG.

$\frac{K_m(nr)}{K_m(nr_{\min})}$ are all limited to values between 0 to 1 for any point in the matrix, and $\left(\frac{r}{r_{\min}}\right)^m$, $\frac{I_m(nr)}{I_m(nr_{\min})}$ are limited to values between 0 to 1 for any point in the fiber, as shown in Tables 1 and 2.

3.4 Trefftz trial displacement fields within the fiber and the matrix

Consider a CG with an embedded unidirectional fiber, with the local cylindrical system given in Fig. 4. The displacement field in the fiber can be assumed in the form of P-N solutions:

$$\mathbf{u}_f = [4(1-\nu_f)\mathbf{B}_f + \mathbf{R}\cdot\nabla\mathbf{B}_f - \mathbf{R}\nabla\cdot\mathbf{B}_f]/(2G_f), \tag{25}$$

where the P-N potential $\mathbf{B}_f$ is expressed in the form of non-singular cylindrical harmonics given in Eq. (23) and scaled as in Table 2. And the displacement field in the matrix is a combination of both singular and non-singular solutions:

$$\mathbf{u}_m = \mathbf{u}_{mi} + \mathbf{u}_{me}, \tag{26}$$

$$\mathbf{u}_{mi} = [4(1-\nu_m)\mathbf{B}_{mi} + \mathbf{R}\cdot\nabla\mathbf{B}_{mi} - \mathbf{R}\nabla\cdot\mathbf{B}_{mi}]/(2G_m), \tag{27}$$

$$\mathbf{u}_{me} = [4(1-\nu_m)\mathbf{B}_{me} - \nabla\mathbf{R}\cdot\mathbf{B}_{me}]/(2G_m), \tag{28}$$

where $\mathbf{B}_{mi}$ is expressed in the form of non-singular cylindrical harmonics given in Eq. (23) scaled as in Table 1, and $\mathbf{B}_{me}$ is expressed in the form of singular cylindrical harmonics given in Eq. (24) scaled as in Table 1.

After defining the displacement fields, the strain and stress expressions can be determined from Eqs. (2) and (3). The derivations of the displacements and stresses are very complicated, and hence are performed using the Wolfram Mathematica 8.0.

It should be noted that the following six rigid-body modes should be deleted in the assumed displacement field:

$$\begin{aligned}
&a_{01} = \{1\ \ 0\ \ 0\}^{\mathrm{T}},\\
&a_{01} = \{0\ \ 1\ \ 0\}^{\mathrm{T}},\\
&a_{01} = \{0\ \ 0\ \ 1\}^{\mathrm{T}},\\
&a_{02} = \{1\ \ 0\ \ 0\}^{\mathrm{T}},\ \ e_{11} = \{0\ \ \ 0\ \ -1\}^{\mathrm{T}},\\
&a_{02} = \{0\ \ 1\ \ 0\}^{\mathrm{T}},\ \ e_{21} = \{0\ \ \ 0\ \ -1\}^{\mathrm{T}},\\
&e_{11} = \{0\ \ 1\ \ 0\}^{\mathrm{T}},\ \ e_{21} = \{-1\ \ 0\ \ \ 0\}^{\mathrm{T}},
\end{aligned} \tag{29}$$

where a_{01}, a_{02}, e_{11}, e_{21} are the coefficients of the cylindrical harmonics shown in Eq. (23).

Moreover, the truncation orders $M = 3$, $N = 1$ are always employed for the singular and non-singular solutions in this study.

Table 1 Scaling of the cylindrical harmonics in the matrix

Non-scaled	z	r^m	r^{-m}	$\sinh(nz)$	$\cosh(nz)$	$I_m(nr)$	$K_m(nr)$
Scaled	$\frac{z}{z_0}$	$\left(\frac{r}{r_{\max}}\right)^m$	$\left(\frac{r}{r_{\min}}\right)^{-m}$	$\frac{\sinh(nz)}{\sinh(nz_0)}$	$\frac{\cosh(nz)}{\cosh(nz_0)}$	$\frac{I_m(nr)}{I_m(nr_{\max})}$	$\frac{K_m(nr)}{K_m(nr_{\min})}$

Table 2 Scaling of the cylindrical harmonics in the fiber

Non-scaled	z	r^m	$\sinh(nz)$	$\cosh(nz)$	$I_m(nr)$
Scaled	$\frac{z}{z_0}$	$\left(\frac{r}{r_{\min}}\right)^m$	$\frac{\sinh(nz)}{\sinh(nz_0)}$	$\frac{\cosh(nz)}{\cosh(nz_0)}$	$\frac{I_m(nr)}{I_m(nr_{\min})}$

4. A new multi-field boundary variational principle and the derived stiffness matrices of CGs

For each CG, by dividing the surfaces into boundary elements, as shown in Fig. 5, the compatible displacement field on $\partial\Omega_m^e$ and $\partial\Omega_f^e$ can be assumed using the conventional nodal shape functions:

$$\tilde{\mathbf{u}} = \widetilde{\mathbf{N}}\mathbf{q}^e. \tag{30}$$

Therefore, a new type of boundary variational functional is developed for the CGs with cylindrical elastic fibers:

$$\Pi(\tilde{\mathbf{u}}, \mathbf{u}_{\mathrm{m}}, \mathbf{u}_{\mathrm{f}}) = \sum_e \left\{ \int_{\partial\Omega_m^e} \frac{1}{2}\mathbf{t}_{\mathrm{m}} \cdot \mathbf{u}_{\mathrm{m}} \mathrm{d}S - \int_{\partial\Omega_m^e} \mathbf{t}_{\mathrm{m}} \cdot \tilde{\mathbf{u}} \mathrm{d}S + \int_{S_t} \bar{\mathbf{t}} \cdot \tilde{\mathbf{u}} \mathrm{d}S \right\}$$
$$+ \sum_e \left\{ \int_{\partial\Omega_f^e} \frac{1}{2}\mathbf{t}_{\mathrm{f}} \cdot \mathbf{u}_{\mathrm{f}} \mathrm{d}S - \int_{\partial\Omega_f^e} \mathbf{t}_{\mathrm{f}} \cdot \tilde{\mathbf{u}} \mathrm{d}S \right\}, \tag{31}$$

in which $\tilde{\mathbf{u}}$ is the assumed compatible displacements at $\partial\Omega_m^e$ and $\partial\Omega_f^e$ given in Eq. (30), $\mathbf{u}_{\mathrm{m}}$ and $\mathbf{u}_{\mathrm{f}}$ are the independently assumed Trefftz displacement fields in terms of the P-N solutions given in Eqs. (25)-(28), and $\mathbf{t}_{\mathrm{m}}$ and $\mathbf{t}_{\mathrm{f}}$ are the surface tractions from $\mathbf{u}_{\mathrm{m}}$ and $\mathbf{u}_{\mathrm{f}}$.

By setting the variation of the functional in Eq. (31) to zero, we can get

$$\mathbf{t}_{\mathrm{m}} = \bar{\mathbf{t}} \ \text{at} \ \mathrm{S}_t^e, \tag{32}$$

$$\mathbf{t}_{\mathrm{f}} = \bar{\mathbf{t}} \ \text{at} \ \mathrm{S}_t^e, \tag{33}$$

$$\mathbf{u}_{\mathrm{m}} = \tilde{\mathbf{u}} \ \text{at} \ \partial\Omega_{\mathrm{m}}^e, \tag{34}$$

$$\mathbf{u}_{\mathrm{f}} = \tilde{\mathbf{u}} \ \text{at} \ \partial\Omega_{\mathrm{f}}^e, \tag{35}$$

$$\mathbf{t}_{\mathrm{m}} + \mathbf{t}_{\mathrm{f}} = \mathbf{0} \ \text{at} \ \Gamma^e, \tag{36}$$

$$\mathbf{t}_{\mathrm{m}}^+ + \mathbf{t}_{\mathrm{m}}^- = \mathbf{0} \ \text{at} \ \rho^e. \tag{37}$$

Using a matrix and vector notation, the displacement field $\mathbf{u}_{\mathrm{m}}$ in Ω_{m}^e and the traction field $\mathbf{t}_{\mathrm{m}}$ at $\partial\Omega_{\mathrm{m}}^e$ can be expressed in terms of the unknown coefficients in the P-N potentials:

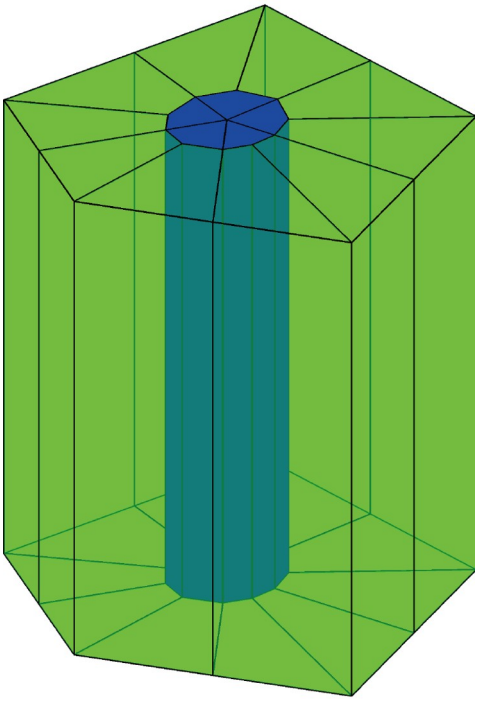

Figure 5 Division of the surface by boundary elements for one CG.

$$\mathbf{u}_{\mathrm{m}} = N_{\mathrm{m}}\boldsymbol{\alpha}^e \ \text{in} \ \Omega_{\mathrm{m}}^e, \tag{38}$$

$$\mathbf{t}_{\mathrm{m}} = \mathbf{R}_{\mathrm{m}}\boldsymbol{\alpha}^e \ \text{at} \ \partial\Omega_{\mathrm{m}}^e. \tag{39}$$

Similarly, the displacement field $\mathbf{u}_{\mathrm{f}}$ in Ω_{f}^e and the traction field $\mathbf{t}_{\mathrm{f}}$ at $\partial\Omega_{\mathrm{f}}^e$ can be expressed as

$$\mathbf{u}_{\mathrm{f}} = N_{\mathrm{f}}\boldsymbol{\beta}^e \ \text{in} \ \Omega_{\mathrm{f}}^e, \tag{40}$$

$$\mathbf{t}_{\mathrm{f}} = \mathbf{R}_{\mathrm{f}}\boldsymbol{\beta}^e \ \text{at} \ \partial\Omega_{\mathrm{f}}^e. \tag{41}$$

Substituting Eqs. (38)-(41) into the boundary variational principle Eq. (31), we have

$$\Pi(\boldsymbol{\alpha}, \boldsymbol{\beta}, \mathbf{q}) = \sum_e \left\{ \frac{1}{2}\boldsymbol{\alpha}^{e\mathrm{T}}\mathbf{H}_{\alpha\alpha}^e\boldsymbol{\alpha}^e - \boldsymbol{\alpha}^{e\mathrm{T}}\mathbf{G}_{\alpha\mathrm{q}}^e\mathbf{q}^e + \mathbf{q}^{e\mathrm{T}}\mathbf{Q}^e \right.$$
$$\left. + \frac{1}{2}\boldsymbol{\beta}^{e\mathrm{T}}\mathbf{H}_{\beta\beta}^e\boldsymbol{\beta}^e - \boldsymbol{\beta}^{e\mathrm{T}}\mathbf{G}_{\beta\mathrm{q}}^e\mathbf{q}^e \right\}, \tag{42}$$

where

$$\mathbf{H}_{\alpha\alpha}^{e}=\int_{\partial\Omega_{\mathrm{m}}^{e}}\mathbf{R}_{\mathrm{m}}^{\mathrm{T}}\mathbf{N}_{\mathrm{m}}\mathrm{d}S, \tag{43}$$

$$\mathbf{H}_{\beta\beta}^{e}=\int_{\partial\Omega_{\mathrm{f}}^{e}}\mathbf{R}_{\mathrm{f}}^{\mathrm{T}}\mathbf{N}_{\mathrm{f}}\mathrm{d}S, \tag{44}$$

$$\mathbf{G}_{\alpha q}^{e}=\int_{\partial\Omega_{\mathrm{m}}^{e}}\mathbf{R}_{\mathrm{m}}^{\mathrm{T}}\widetilde{\mathbf{N}}\mathrm{d}S, \tag{45}$$

$$\mathbf{G}_{\beta q}^{e}=\int_{\partial\Omega_{\mathrm{f}}^{e}}\mathbf{R}_{\mathrm{f}}^{\mathrm{T}}\widetilde{\mathbf{N}}\mathrm{d}S, \tag{46}$$

$$\mathbf{Q}^{e}=\int_{S_{\mathrm{t}}^{e}}\widetilde{\mathbf{N}}^{\mathrm{T}}\bar{\mathbf{t}}\mathrm{d}S. \tag{47}$$

The vanishing of the first variation of the functional in Eq. (42) leads to

$$\begin{aligned}\delta\Pi(\boldsymbol{\alpha},\boldsymbol{\beta},\mathbf{q})=\sum_{e}\Big\{&\delta\boldsymbol{\alpha}^{e\mathrm{T}}\left(\mathbf{H}_{\alpha\alpha}^{e}\boldsymbol{\alpha}^{e}-\mathbf{G}_{\alpha q}^{e}\mathbf{q}^{e}\right)+\delta\mathbf{q}^{e\mathrm{T}}\left(\mathbf{Q}^{e}-\mathbf{G}_{\alpha q}^{e\mathrm{T}}\boldsymbol{\alpha}^{e}\right.\\&\left.-\mathbf{G}_{\beta q}^{e\mathrm{T}}\boldsymbol{\beta}^{e}\right)+\delta\boldsymbol{\beta}^{e\mathrm{T}}\left(\mathbf{H}_{\beta\beta}^{e}\boldsymbol{\beta}^{e}-\mathbf{G}_{\beta q}^{e}\mathbf{q}^{e}\right)\Big\}=0,\end{aligned} \tag{48}$$

which can be re-written as

$$\delta\begin{Bmatrix}\mathbf{q}^{e}\\\boldsymbol{\alpha}^{e}\\\boldsymbol{\beta}^{e}\end{Bmatrix}^{\mathrm{T}}\begin{bmatrix}\mathbf{0}&\mathbf{G}_{\alpha q}^{e\mathrm{T}}&\mathbf{G}_{\beta q}^{e\mathrm{T}}\\-\mathbf{G}_{\alpha q}^{e}&\mathbf{H}_{\alpha\alpha}^{e}&\mathbf{0}\\-\mathbf{G}_{\beta q}^{e}&\mathbf{0}&\mathbf{H}_{\beta\beta}^{e}\end{bmatrix}\begin{Bmatrix}\mathbf{q}^{e}\\\boldsymbol{\alpha}^{e}\\\boldsymbol{\beta}^{e}\end{Bmatrix}=\delta\begin{Bmatrix}\mathbf{q}^{e}\\\boldsymbol{\alpha}^{e}\\\boldsymbol{\beta}^{e}\end{Bmatrix}^{\mathrm{T}}\begin{Bmatrix}\mathbf{Q}^{e}\\\mathbf{0}\\\mathbf{0}\end{Bmatrix}. \tag{49}$$

The finite element equations are thus derived as

$$\begin{aligned}&\sum_{e}\delta\mathbf{q}^{e\mathrm{T}}\left(\mathbf{G}_{\mathrm{\alpha q}}^{e\mathrm{T}}\mathbf{H}_{\mathrm{\alpha\alpha}}^{e\ -1}\mathbf{G}_{\mathrm{aq}}^{e}+\mathbf{G}_{\mathrm{\beta q}}^{e\mathrm{T}}\mathbf{H}_{\mathrm{\beta\beta}}^{e\ -1}\mathbf{G}_{\mathrm{\beta q}}^{e}\right)\mathbf{q}^{e}\\&=\sum_{e}\delta\mathbf{q}^{e\mathrm{T}}\mathbf{Q}^{e},\end{aligned} \tag{50}$$

where $\sum$ denotes the assembly of stiffness matrices.

And the following equations can be used to compute the coefficients in the matrix and in the fiber:

$$\begin{aligned}\boldsymbol{\alpha}^{e}&=\mathbf{H}_{\alpha\alpha}^{e\ -1}\mathbf{G}_{\alpha q}^{e}\mathbf{q}^{e},\\\boldsymbol{\beta}^{e}&=\mathbf{H}_{\beta\beta}^{e\ -1}\mathbf{G}_{\beta q}^{e}\mathbf{q}^{e}.\end{aligned} \tag{51}$$

5. Numerical examples

In this section, numerical examples are given to test the performance of the CGs developed in this study. All the examples were run on a desktop PC with a AMD R7 processor and a 16G RAM.

5.1 Verifying the effects of scaling the Trefftz functions

Firstly, the necessity for scaling the P-N potentials by using characteristic lengths is studied. Figure 6 shows the geometry of the CG. The dimension of the CG considered here is $L\times W\times H=40\times40\times60$ μm, and the radius of the fiber is $R=2$ μm. The material properties of matrix and fiber are $E_m=1$ GPa, $\nu_m=0.2$, $E_f=2$ GPa, $\nu_f=0.3$, respectively. The stiffness matrix is calculated with and without the scaling of the Trefftz trial functions by characteristic lengths. The condition numbers of the coefficient matrices used to relate $\boldsymbol{\alpha}^{e}$ and $\boldsymbol{\beta}^{e}$ to $\mathbf{q}^{e}$, i.e., of the matrices $\mathbf{H}_{\alpha\alpha}^{e}$ and $\mathbf{H}_{\beta\beta}^{e}$ given in Eqs. (43) and (44), which need to be inverted to calculate the stiffness matrix, are listed in Table 3. It can be noticed that the condition numbers are reduced significantly by scaling the cylindrical harmonics with the use of characteristic lengths.

5.2 The objectivity test and the patch test

For the same CG as given in Fig. 6, the objectivity test and the Patch test are conducted. The objectivity of the stiffness matrix of the derived CGs is verified by checking that the eigenvalues of the stiffness matrices stay the same with rotated coordinate systems. And the Patch test is performed by specifying the same material properties for the matrix and the fiber ($E=1$, $\nu=0.25$), and applying a tensile/shear load. The computed solution by the CG can reproduce the analytical linear displacement field with a relative error of less than 10^{-10}.

5.3 Verifying the accuracy of the computed microscopic stresses

Consider that an infinite domain with an infinitely long fiber is subjected to a transverse remote tension. The exact so-

Table 3 Condition numbers of the coefficient matrices $\mathbf{H}_{\alpha\alpha}^{e}$ and $\mathbf{H}_{\beta\beta}^{e}$

	$\mathbf{H}_{\alpha\alpha}^{e}$	$\mathbf{H}_{\beta\beta}^{e}$
Not scaled	1.9642×10^{29}	1.9981×10^{27}
Scaled	8.6089×10^{4}	3.7710×10^{5}

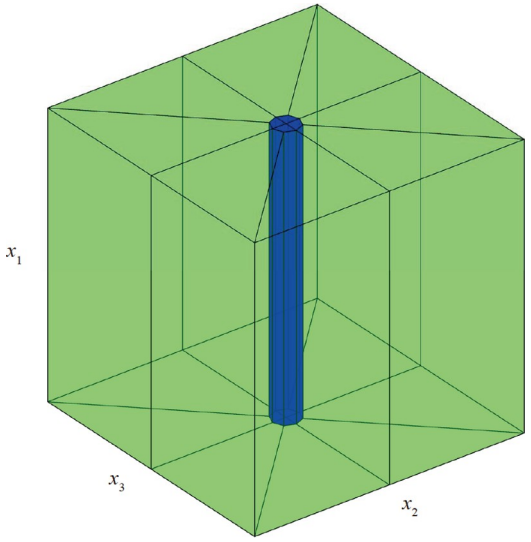

Figure 6 CG used for the test of condition numbers.

lutions can be found in Refs. [10,39]. A single CG with the same geometry as that in Fig. 6 is used. The material properties of matrix and fiber are $E_m = 1$ GPa, $\nu_m = 0.25$, $E_f = 2$ GPa, $\nu_f = 0.3$, respectively. A remote tension is applied in x_2 direction, i.e., $P = 100$ MPa. The computed σ_{22} and σ_{33} are in good agreement with those by the exact solutions, as shown in Figs. 7 and 8.

Additionally, a fiber embedded in an infinite domain that is subjected to a longitudinal remote tensile strain is also studied. The exact solutions in the fiber and the matrix are given in Ref. [40]. A CG which is the same as that in the above example is used, and the radius of the fiber is $R = 4$ μm. A longitudinal uniform strain field $\varepsilon_{11} = 0.1\%$ is applied in x_1 direction. Figures 9 and 10 show that the CG

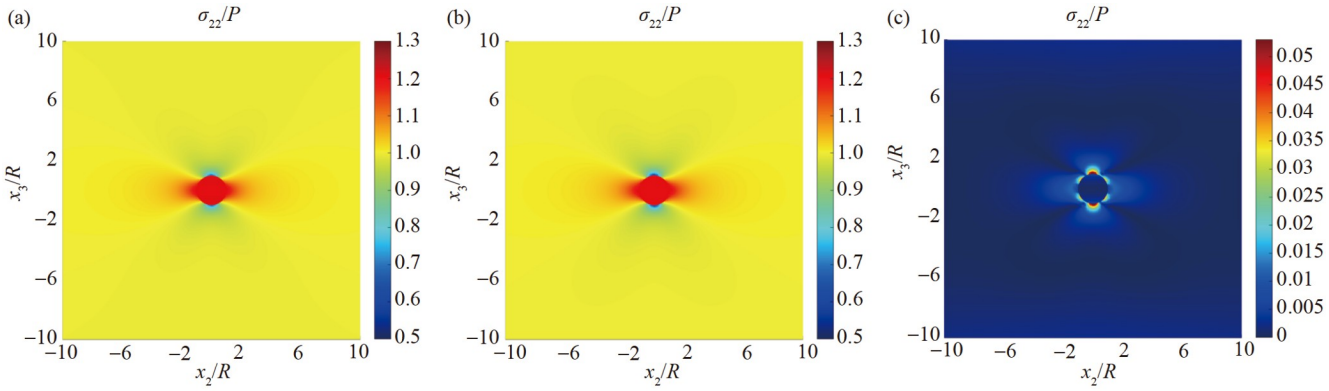

Figure 7 σ_{22}/P generated by (a) the CG and (b) the exact solutions, and (c) the errors between the CG results and the exact solutions, for a fiber embedded in an infinite domain under remote transverse tension.

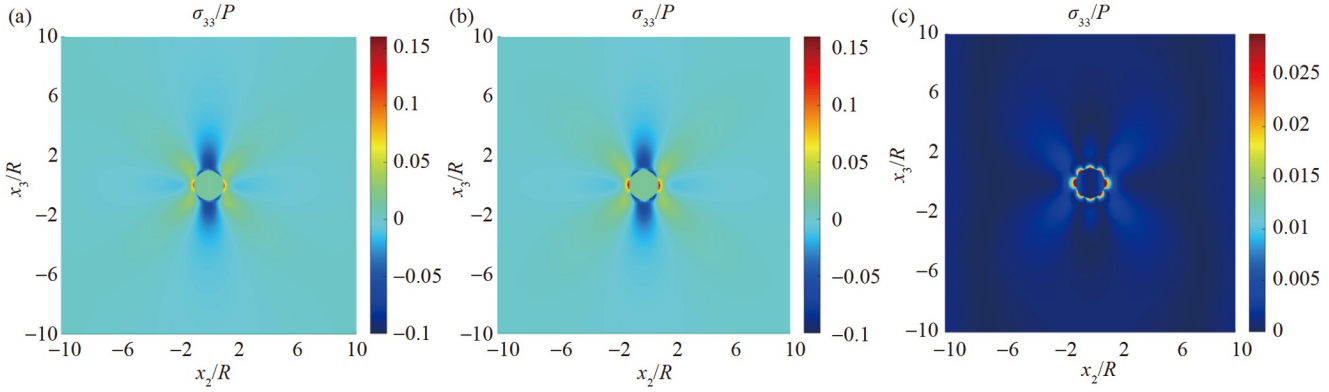

Figure 8 σ_{33}/P generated by (a) the CG and (b) the exact solutions, and (c) the errors between the CG results and the exact solutions, for a fiber embedded in an infinite domain under remote transverse tension.

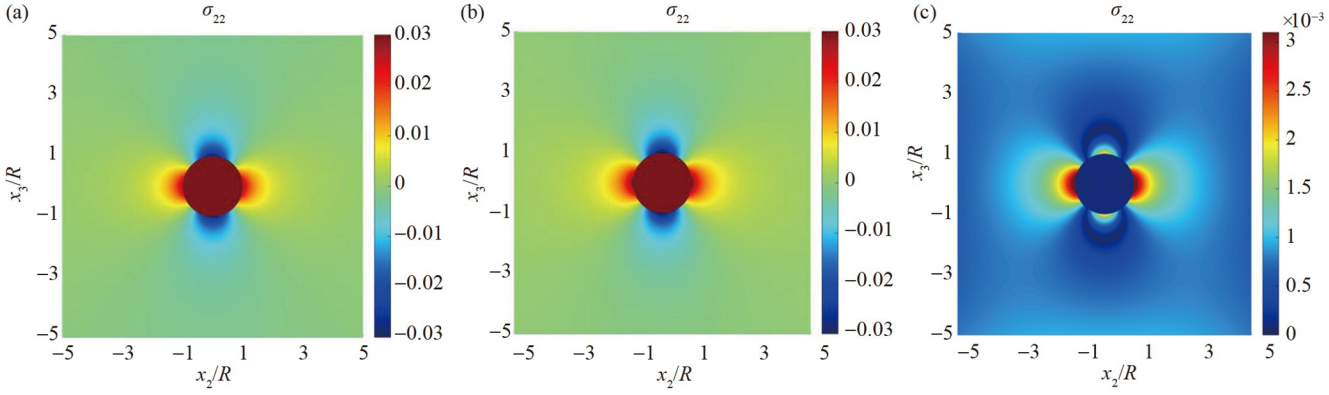

Figure 9 σ_{22} generated by (a) the CG and (b) the exact solutions, and (c) the errors between the CG results and the exact solutions, for a fiber embedded in an infinite domain under longitudinal tension.

gives very accurate solutions, compared with the exact solutions.

Finally, by using the same model, a fiber embedded in an infinite domain that is subjected to a longitudinal remote shear is also studied. The exact solutions can be found in Ref. [41]. And the same CG is used. A constant shear stress $\tau_{12}^{\infty} = 100$ MPa is applied to the surface of the CG. Figures 11 and 12 show that the computed results are in good agreement with the exact solutions.

5.4 Prediction of the effective moduli of fiber composites

We also study the equivalent moduli of a fiber composite by CGs. The material properties of the glass fiber and the polymer matrix are $E_f = 72.4$ GPa, $v_f = 0.22$, $E_m = 3.5735$ GPa, $v_m = 0.345$, respectively. A single CG is used and the radius of the fiber varies with the volume fraction. Periodic boundary conditions are applied. The obtained equivalent moduli E_{11}, E_{22}, G_{12}, G_{23} are compared with experimental results

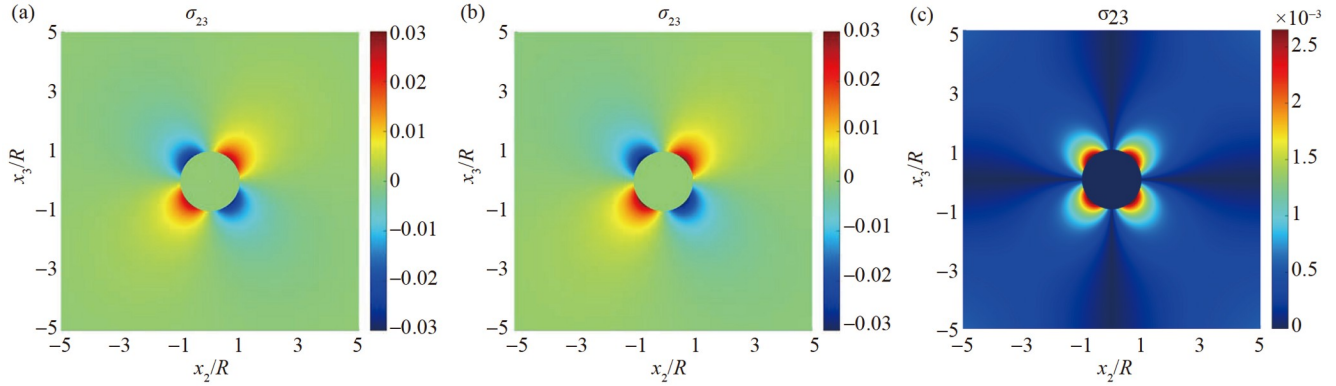

Figure 10 σ_{23} generated by (a) the CG and (b) the exact solutions, and (c) the errors between the CG results and the exact solutions, for a fiber embedded in an infinite domain under longitudinal tension.

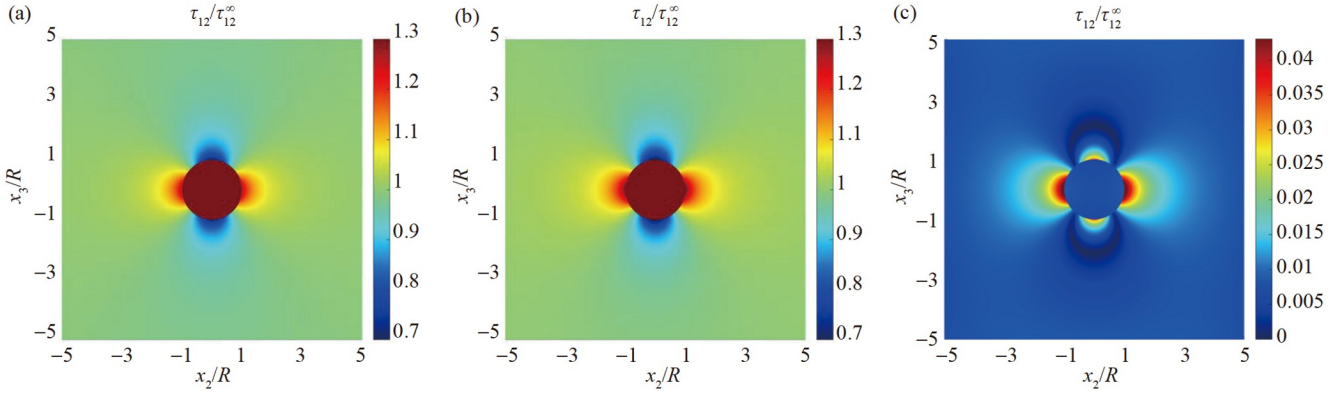

Figure 11 $\tau_{12}/\tau_{12}^{\infty}$ generated by (a) the CG and (b) the exact solutions, and (c) the errors between the CG results and the exact solutions, for a fiber embedded in an infinite domain under longitudinal shear.

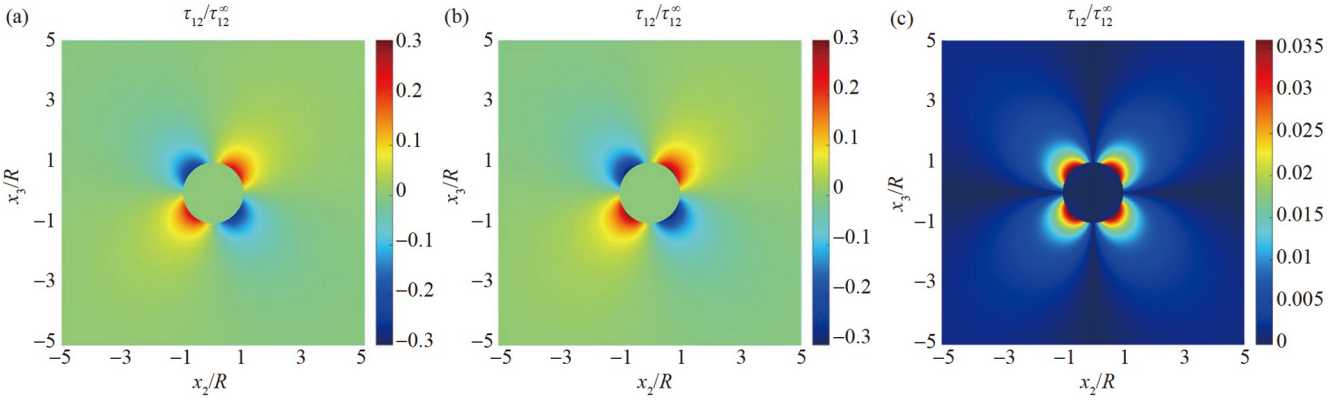

Figure 12 $\tau_{13}/\tau_{12}^{\infty}$ generated by (a) the CG and (b) the exact solutions, and (c) the errors between the CG results and the exact solutions, for a fiber embedded in an infinite domain under longitudinal shear.

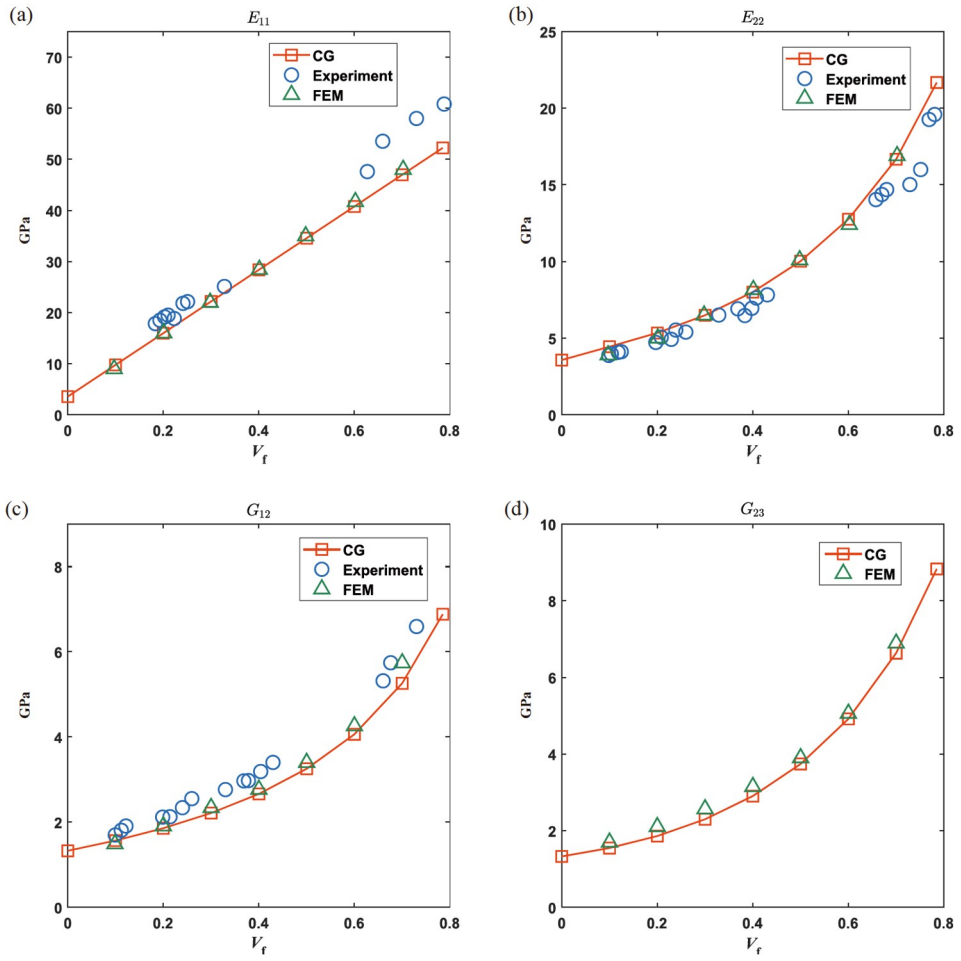

Figure 13 Variation of the (a) longitudinal Young's modulus E_{11}, (b) transverse Young's modulus E_{22}, (c) longitudinal shear modulus G_{12}, (d) transverse shear modulus G_{23}, with the volume fraction of the glass fiber.

in Ref. [42]. Figure 13 shows that although only one CG is employed, the computed transverse and longitudinal effective moduli all agree well with the FEM and experimental results.

5.5 CGs with a large number of fibers with parallel computation

A RVE with a large number of fibers is simulated. Figure 14 shows a RVE containing n randomly-distributed fibers. The material properties of the glass fiber and the polymer matrix are the same as the above example, and a uniform traction $P = 100$ MPa is applied in x_2 direction. Figures 15-20 show the computed maximum principal stress and strain energy density distribution for three RVEs containing 25 fibers, with the volume fractions of 8%, 33%, and 63%, respectively. It can be shown that while the maximum principal stress and strain energy density distribution in fibers is relatively uniform, a highly varying stress and strain energy density can be observed in the matrix.

In order to demonstrate the efficiency of the CGs when

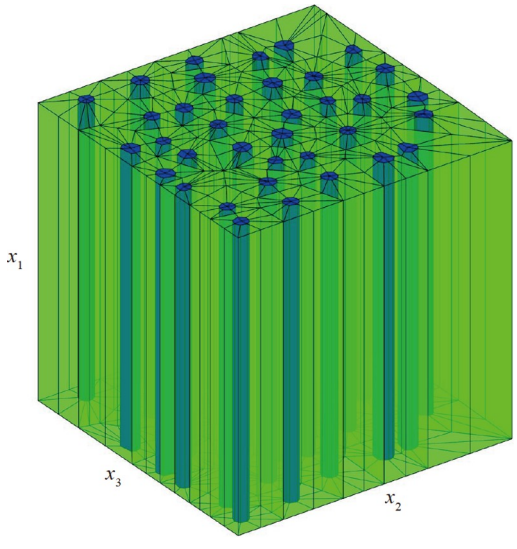

Figure 14 A RVE containing n randomly-distributed fibers.

modeling a RVE with a large number of fibers, two RVEs containing 250 and 2500 CGs are modeled, and parallel computation is implemented to further accelerate the ana-

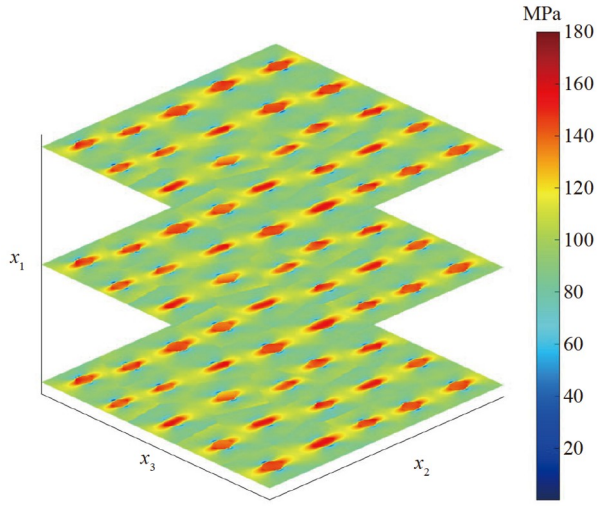

Figure 15 Distribution of maximum principal stress in the RVE containing 25 fibers, with the fiber volume fraction of 8%.

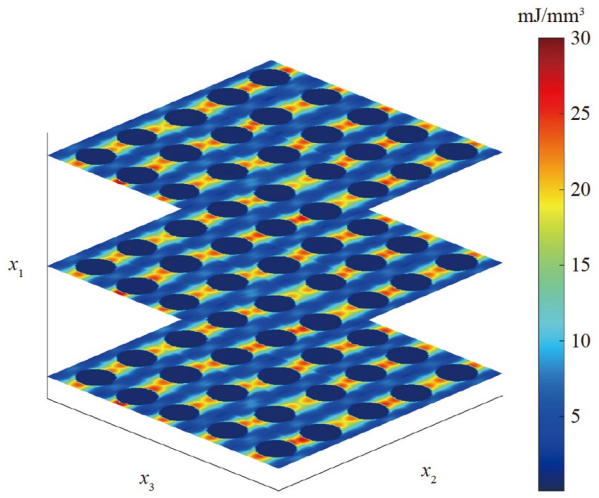

Figure 18 Distribution of strain energy density in the RVE containing 25 fibers, with the fiber volume fraction of 33%.

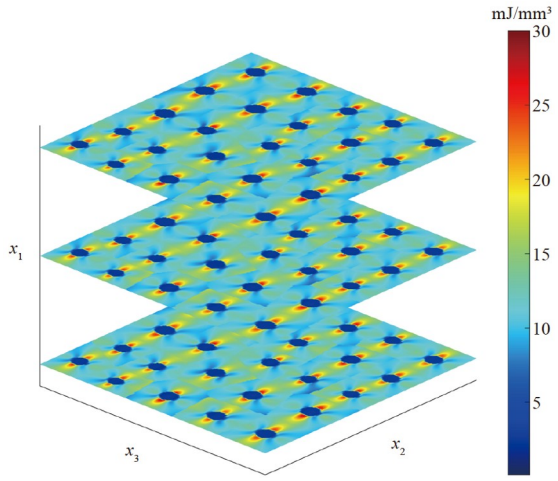

Figure 16 Distribution of strain energy density in the RVE containing 25 fibers, with the fiber volume fraction of 8%.

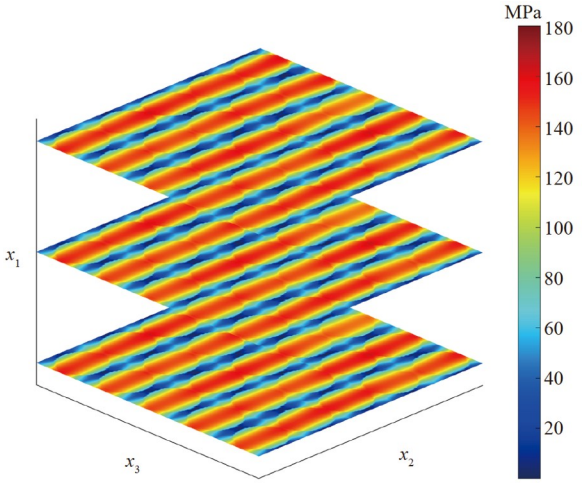

Figure 19 Distribution of maximum principal stress in the RVE containing 25 fibers, with the fiber volume fraction of 63%.

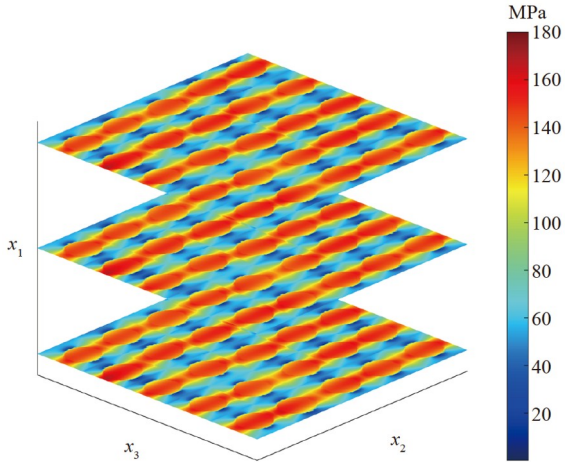

Figure 17 Distribution of maximum principal stress in the RVE containing 25 fibers, with the fiber volume fraction of 33%.

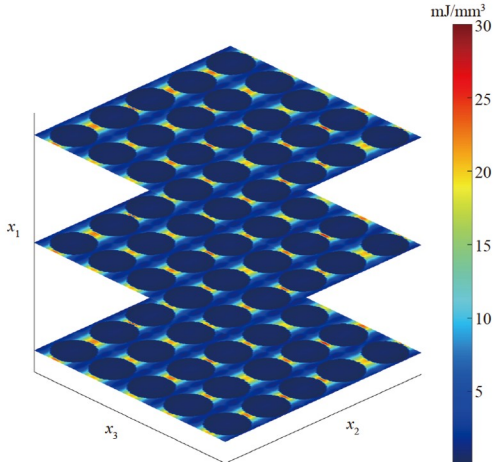

Figure 20 Distribution of strain energy density in the RVE containing 25 fibers, with the fiber volume fraction of 63%.

lysis. Detailed process of parallelization is similar to that of Ref. [34]. Because most of the computational time is spent on calculating the stiffness matrix of each CG, we simply assign each of n threads to compute stiffness matrices of $1/n$ of the CGs. Figures 21-24 show the computed maximum principal stress and strain energy density distribution for the RVEs with 250 and 2500 fibers, respectively. Using a desktop PC with an AMD R7 processor and a 16G RAM, the time required for solving the three RVEs with 25, 250, 2500 fibers with/without parallel algorithm is given in Table 4. It shows that parallelization can significantly reduce the computational time, and a RVE with 2500 fibers can be simulated within 10 hours using a regular desktop PC.

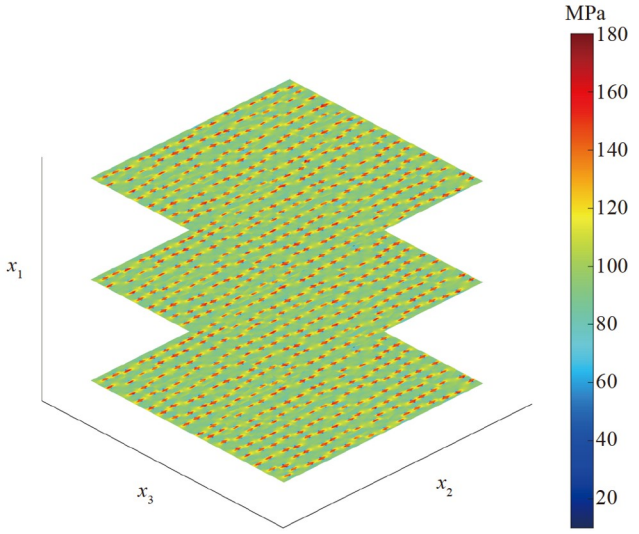

Figure 21 Distribution of maximum principal stress in the RVE containing 250 fibers.

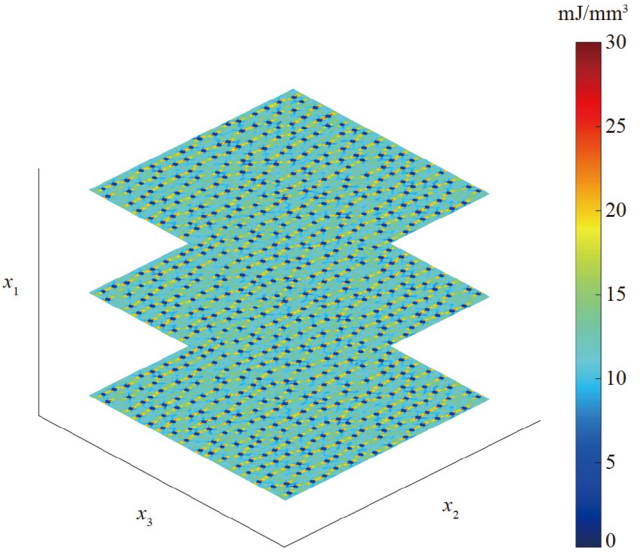

Figure 22 Distribution of strain energy density in the RVE containing 250 CGs.

Table 4 Time required for the CGs with/without parallel computation

	25	250	2500
Without parallel computation (s)	2678.19	25561.12	254985.36
With parallel computation (s)	423.12	3778.24	34951.12

6. Conclusions

In this study, CGs with embedded fibers are developed for the first time, as a power micromechanical tool for modeling fiber composites. Different to CGs with embedded particles, on the one hand, the trial displacement fields within the CGs are assumed with cylindrical harmonics as P-N potentials, and a new scaling method for the cylindrical harmonics has been proposed to successfully avoid the problem of ill-conditioning; on the other hand, a new multi-field boundary variational principle has been developed to derive the

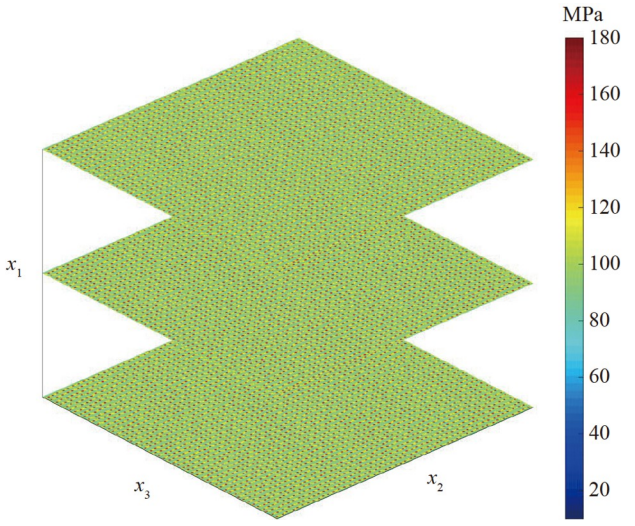

Figure 23 Distribution of maximum principal stress in the RVE containing 2500 CGs.

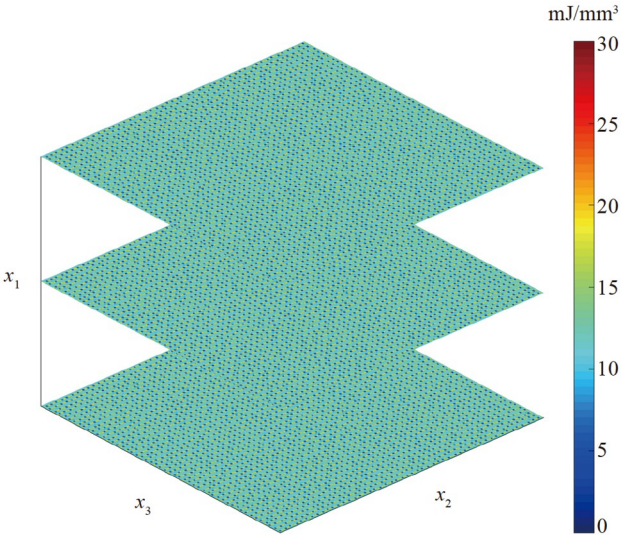

Figure 24 Distribution of strain energy density in the RVE containing 2500 CGs.

stiffness matrices of the CGs with embedded fibers.

Numerical examples demonstrate that the developed CGs can accurately capture the localized stress distributions under various loadings and estimate the effective material properties of fiber reinforced composites, by comparing the computational results with exact solutions and experimental results in the literature. Moreover, with the use of simple parallelization, the time required for CGs is significantly decreased. It was shown that solving a RVE with 2500 randomly distributed unidirectional fibers took less than 10 hours on an 8-core desktop PC. Thus, we consider that the CG developed in this study is an accurate and efficient tool for the micromechanical modeling of fiber composites.

It is expected that such a powerful micromechanical tool can be coupled with FEM in large-scales and employed in the multi-scale analysis framework for the integrated design of composite materials and structures. For example, based on the proposed CGs and the homogenization at the micro-scale, the equivalent moduli of fiber composites (such as single-layer laminas) can be calculated; and then by using the FEM at meso- and macro-scale (such as laminates and 3D braided composites), the deformation/buckling of large-scale composite beam/shells that are typically used in lightweight structures can be simulated. This will be demonstrated in our future studies.

Appendix

By assuming $\psi = f(r)g(\theta)h(z)$ and substituting it into Eq. (19), it can be shown that $f(r)$, $g(\theta)$, $h(z)$ should satisfy the following equation:

$$\frac{1}{rf}\frac{\partial}{\partial r}\left(r\frac{\partial f}{\partial r}\right)+\frac{1}{r^2 g}\frac{\partial^2 g}{\partial \theta^2}+\frac{1}{h}\frac{\partial^2 h}{\partial z^2}=0. \tag{A1}$$

Using λ as the separating constant, the z-dependent term is re-written as

$$\frac{1}{rf}\frac{\partial}{\partial r}\left(r\frac{\partial f}{\partial r}\right)+\frac{1}{r^2 g}\frac{\partial^2 g}{\partial \theta^2}=-\frac{1}{h}\frac{\partial^2 h}{\partial z^2}=\lambda. \tag{A2}$$

For $-\frac{1}{h}\frac{\partial^2 h}{\partial z^2}=\lambda$, the characteristic polynomial is $r^2+\lambda$, the vanishing of which leads to $r=\pm\sqrt{-\lambda}$. Thus, the expression of $h(z)$ needs to be discussed in three cases according to the value of λ:

(1) If $\lambda<0$, let $\lambda=-n^2$, and we have

$h(z)=E_n\cosh(nz)+F_n\sinh(nz)$.

(2) If $\lambda=0$, then $h(z)=E_0+F_0 z$.

(3) If $\lambda>0$, let $\lambda=n^2$, $r=\pm in$, and we have

$h(z)=E_{-n}\cos(nz)+F_{-n}\sin(nz)$.

Equation (A2) can be used to derive

$$\frac{r}{f}\frac{\partial}{\partial r}\left(r\frac{\partial f}{\partial r}\right)-\lambda r^2=-\frac{1}{g}\frac{\partial^2 g}{\partial \theta^2}=\kappa \tag{A3}$$

by using κ as the separating constant.

For $-\frac{1}{g}\frac{\partial^2 g}{\partial \theta^2}=\kappa$, the characteristic polynomial is $r^2+\kappa=0$, and $r=\pm\sqrt{-\kappa}$. Considering that $g(\theta)$ is periodic, the expression of $g(\theta)$ needs to be discussed in two cases according to the value of κ:

(1) If $\kappa=0$, then $g(\theta)=C_0$.

(2) If $\kappa>0$, let $\kappa=m^2$, $\kappa=\pm im$, and we have $g(\theta)=C_{-m}\cos(m\theta)+F_{-m}\sin(m\theta)$.

Then, the radial solution in r direction is governed by

$$\frac{\partial^2 f}{\partial r^2}+\frac{1}{r}\frac{\partial f}{\partial r}+\left(-\lambda-\frac{\kappa}{r^2}\right)f=0, \tag{A4}$$

whose solutions are related to the values of both λ and κ:

(1) If $\lambda=0$ and $\kappa=0$, then $f(r)=A_{00}+B_{00}\ln r$.

(2) If $\lambda=0$ and $\kappa>0$ ($\kappa=m^2$), then

$f(r)=A_{0m}r^m+B_{0m}r^{-m}$.

(3) If $\lambda<0$ ($\lambda=-n^2$) and $\kappa>0$ ($\kappa=m^2$), we have

$$\frac{\partial^2 f}{\partial r^2}+\frac{1}{r}\frac{\partial f}{\partial r}+\left(n^2-\frac{m^2}{r^2}\right)f=0, \tag{A5}$$

which is the Bessel differential equation, and the solutions are Bessel functions of first and second kinds:

$$f(r)=A_{-mn}J_m(nr)+B_{-mn}Y_m(nr), \tag{A6}$$

where J_m and Y_m denote as the Bessel function of the first kind and the second kind, respectively.

(4) If $\lambda<0$ and $\kappa=0$, then

$f(r)=A_{-n0}J_0(nr)+B_{-n0}Y_0(nr)$.

(5) If $\lambda>0(\lambda=n^2)$ and $\kappa>0(\kappa=m^2)$, we have the modified Bessel differential equation:

$$\frac{\partial^2 f}{\partial r^2}+\frac{1}{r}\frac{\partial f}{\partial r}+\left(-n^2-\frac{m^2}{r^2}\right)f=0, \tag{A7}$$

the solutions of which are modified Bessel functions of first and second kinds:

$$f(r)=A_{mn}I_m(nr)+B_{mn}K_m(nr), \tag{A8}$$

where I_m and K_m denote the modified Bessel function of the first kind and the second kind, respectively.

(6) If $\lambda>0$ and $\kappa=0$, we have

$f(r)=A_{n0}I_0(nr)+B_{n0}K_0(nr)$.

Finally, the analytical expression of ψ can be written in the form of Eqs. (23) and (24) .

Conflict of interest *On behalf of all authors, the corresponding author states that there is no conflict of interest.*

Author contributions *Yezeng Huang designed the research. Yezeng Huang and Junbo Wang wrote the first draft of the manuscript. Yezeng Huang and Guannan Wang provided the computer code and the supporting algorithms. Mingjing Li and Guannan Wang helped organize the manu-*

script. Leiting Dong and Satya N. Atluri revised and edited the final version.

Acknowledgements *This work was supported by the National Natural Science Foundation of China (Grant Nos. 12072011 and 12102023).*

1 B. Qiu, X. Zhang, S. Xia, T. Sun, Y. Ling, S. Zhou, H. Guang, Y. Chen, Z. Xu, M. Liang, and H. Zou, Magnetic graphene oxide/carbon fiber composites with improved interfacial properties and electromagnetic interference shielding performance, Compos. Part A-Appl. Sci. Manuf. **155**, 106811 (2022).

2 N. R. J. Hynes, N. J. Vignesh, J. T. W. Jappes, P. S. Velu, C. Barile, M. A. Ali, M. U. Farooq, and C. I. Pruncu, Effect of stacking sequence of fibre metal laminates with carbon fibre reinforced composites on mechanical attributes: Numerical simulations and experimental validation, Compos. Sci. Tech. **221**, 109303 (2022).

3 Z. Huang, K. Fu, Y. Li, and C. Yan, Development of impact resistant 3D printed multi-layer carbon fibre reinforced composites by structural design, Acta Mech. Sin. **38**, 121428 (2022).

4 H. Xin, A. Mosallam, J. A. F. O. Correia, Y. Liu, J. He, and Y. Sun, Material-structure integrated design optimization of GFRP bridge deck on steel girder, Structures **27**, 1222 (2020).

5 R. Hill, Theory of mechanical properties of fibre-strengthened materials: I. Elastic behaviour, J. Mech. Phys. Solids **12**, 199 (1964).

6 Z. Hashin, On elastic behaviour of fibre reinforced materials of arbitrary transverse phase geometry, J. Mech. Phys. Solids **13**, 119 (1965).

7 R. Hill, Theory of mechanical properties of fibre-strengthened materials—III. self-consistent model, J. Mech. Phys. Solids **13**, 189 (1965).

8 Y. Benveniste, G. J. Dvorak, and T. Chen, Stress fields in composites with coated inclusions, Mech. Mater. **7**, 305 (1989).

9 T. Mori, and K. Tanaka, Average stress in matrix and average elastic energy of materials with misfitting inclusions, Acta Metall. **21**, 571 (1973).

10 J. D. Eshelby, The determination of the elastic field of an ellipsoidal inclusion, and related problems, Proc. R. Soc. Lond. A **241**, 376 (1957).

11 M. Ferrari, Asymmetry and the high concentration limit of the Mori-Tanaka effective medium theory, Mech. Mater. **11**, 251 (1991).

12 Q. Guo, W. Yao, W. Li, and N. Gupta, Constitutive models for the structural analysis of composite materials for the finite element analysis: A review of recent practices, Compos. Struct. **260**, 113267 (2021).

13 S. Bahl, and A. K. Bagha, Finite element modeling and simulation of the fiber-matrix interface in fiber reinforced metal matrix composites, Mater. Today-Proc. **39**, 70 (2021).

14 M. Katouzian, S. Vlase, and M. L. Scutaru, Finite element method-based simulation creep behavior of viscoelastic carbon-fiber composite, Polymers **13**, 1017 (2021).

15 C. Stephen, S. R. Behara, B. Shivamurthy, R. Selvam, S. Kannan, and M. Abbadi, Finite element study on the influence of fiber orientation on the high velocity impact behavior of fiber reinforced polymer composites, Int. J. Interact. Des. Manuf. **16**, 459 (2022).

16 F. Yang, Z. Li, Z. Zhuang, and Z. Liu, Evaluating the blast mitigation performance of hard/soft composite structures through field explosion experiment and numerical analysis, Acta Mech. Sin. **38**, 121238 (2022).

17 A. G. Adeniyi, S. A. Adeoye, D. V. Onifade, and J. O. Ighalo, Multi-scale finite element analysis of effective elastic property of sisal fiber-reinforced polystyrene composites, Mech. Adv. Mater. Struct. **28**, 1245 (2021).

18 X. Wang, H. Li, T. Yang, Z. Zhang, C. Zheng, W. Wang, D. Zhang, and K. Qian, Multi-scale strength and buckling analysis of 3D woven composite spherical shells subjected to hydrostatic pressure, J. Industrial Textiles **51**, 6236S (2022).

19 M. Chen, and Q. Liu, Multi-scale modelling of progressive damage and failure behaviour of 2D woven SiC/SiC composites, Ceram. Int. **47**, 28821 (2021).

20 E. Kheng, R. D'Mello, and A. Waas, A multi-scale model for the tensile failure of twill textile composites, Compos. Struct. **307**, 116614 (2023).

21 H. Dang, P. Liu, Y. Zhang, Z. Zhao, L. Tong, C. Zhang, and Y. Li, Theoretical prediction for effective properties and progressive failure of textile composites: A generalized multi-scale approach, Acta Mech. Sin. **37**, 1222 (2021).

22 A. Bhaduri, A. Gupta, and L. Graham-Brady, Stress field prediction in fiber-reinforced composite materials using a deep learning approach, Compos. Part B-Eng. **238**, 109879 (2022).

23 S. A. Tabatabaei, S. V. Lomov, and I. Verpoest, Assessment of embedded element technique in meso-FE modelling of fibre reinforced composites, Compos. Struct. **107**, 436 (2014).

24 M. Mahdi, and L. Zhang, An adaptive three-dimensional finite element algorithm for the orthogonal cutting of composite materials, J. Mater. Process. Tech. **113**, 1 (2001).

25 S. Ghosh, and R. L. Mallett, Voronoi cell finite elements, Comput. Struct. **50**, 33 (1994).

26 S. Ghosh, K. Lee, and S. Moorthy, Multiple scale analysis of heterogeneous elastic structures using homogenization theory and voronoi cell finite element method, Int. J. Solids Struct. **32**, 27 (1995).

27 T. H. H. Pian, Derivation of element stiffness matrices by assumed stress distributions, AIAA J. **2**, 1333 (1964).

28 P. Raghavan, and S. Ghosh, A continuum damage mechanics model for unidirectional composites undergoing interfacial debonding, Mech. Mater. **37**, 9 (2005).

29 S. Ghosh, and S. Moorthy, Three dimensional Voronoi cell finite element model for microstructures with ellipsoidal heterogeneties, Comput. Mech. **34**, 510 (2004).

30 R. Zhang, T. Wang, and R. Guo, Modeling of interphases in multiple heterogeneities reinforced composites using Voronoi cell finite elements, Acta Mech. Sin. **36**, 887 (2020).

31 S. Li, and S. Ghosh, Modeling interfacial debonding and matrix cracking in fiber reinforced composites by the extended Voronoi cell FEM, Finite Elem. Anal. Des. **43**, 397 (2007).

32 L. Dong, and S. N. Atluri, Development of 3D T-Trefftz Voronoi cell finite elements with/without spherical voids \&/or elastic/rigid inclusions for micromechanical modeling of heterogeneous materials, CMC-Comput. Mater. Con. **29**, 2 (2012).

33 L. Dong, and S. N. Atluri, Development of 3D Trefftz Voronoi cells with ellipsoidal voids \&/or elastic/rigid inclusions for micromechanical modeling of heterogeneous materials, CMC-Comput. Mater. Con. **30**, 1 (2012).

34 J. Wang, P. Yan, L. Dong, and S. N. Atluri, Direct numerical simulation of complex nano-structured composites, considering interface stretching and bending effects, using nano-computational grains, Int. J. Numer. Methods Eng. **122**, 1476 (2021).

35 G. Wang, L. Dong, J. Wang, and S. Atluri, Three-dimensional Trefftz computational grains for the micromechanical modeling of heterogeneous media with coated spherical inclusions, J. Mech. Mater. Struct. **13**, 505 (2018).

36 P. L. Bishay, L. Dong, and S. N. Atluri, Multi-physics computational grains (MPCGs) for direct numerical simulation (DNS) of piezoelectric composite/porous materials and structures, Comput. Mech. **54**,

1129 (2014).
37 Y. Huang, G. Wang, L. Dong, and S. N. Atluri, 3D viscoelastic computational grains with spherical inclusions with or without interphases/coatings for micromechanical modeling of heterogeneous materials, Int. J. Numer. Methods Eng. **122**, 4966 (2021).
38 L. Ai, Theory of Elasticity, 4th ed., translated by Belyaev (Springer, Berlin, 2005).
39 J. D. Eshelby, The elastic field outside an ellipsoidal inclusion, Proc. R. Soc. Lond. A **252**, 561 (1959).
40 Z. H. Tong, S. H. Lo, C. P. Jiang, and Y. K. Cheung, An exact solution for the three-phase thermo-electro-magneto-elastic cylinder model and its application to piezoelectric-magnetic fiber composites, Int. J. Solids Struct. **45**, 5205 (2008).
41 C. P. Jiang, Y. L. Xu, Y. K. Cheung, and S. H. Lo, A rigorous analytical method for doubly periodic cylindrical inclusions under longitudinal shear and its application, Mech. Mater. **36**, 3 (2004).
42 P. M. No, Finite Element Method: Simulation, Numerical Analysis and Solution Techniques (IntechOpen, London, 2018).

基于三维纤维计算晶粒的纤维复合材料直接细观力学建模

黄业增, 王俊博, 李明净, 王冠楠, 董雷霆, Satya N. Atluri

摘要 面向纤维复合材料与结构的优化设计需要, 建立高效准确的纤维复材细观力学仿真工具具有重要意义. 本文首次提出了包含内嵌纤维的三维计算晶粒(computational grains), 用于纤维增强复合材料的直接细观力学建模. 基于所开发的纤维计算晶粒方法, 可以直接构造含有多根随机分布纤维的代表性体积单元(RVE). 此外, 本文提出了一种基于缩放柱调和函数的Papkovich-Neuber解来表征纤维和基体中独立的Trefftz试函数位移场, 并且开发了一种新的多场边界变分原理来计算纤维计算晶粒的刚度矩阵. 数值算例表明, 对于内嵌大量随机分布纤维的RVE, 纤维计算晶粒不需要构造复杂的网格, 即可快速计算RVE的精确应力场, 并预测其有效力学性能. 此外, 这也是内嵌纤维的三维有限元单元的首次提出.